Design and Construction of a Two-Stage Thermoacoustic Electricity Generator with Push-Pull Linear Alternator

Ahmed Hamood [1], Artur J. Jaworski [2 *], Xiaoan Mao [1] and Kevin Simpson [3]

[1] Faculty of Engineering, University of Leeds, Leeds LS2 9JT, United Kingdom

[2] School of Computing and Engineering, University of Huddersfield, Huddersfield HD1 3DH, United Kingdom

[3] European Thermodynamics Ltd, 8 Priory Business Park, Kibworth, Leicestershire, LE8 0RX, United Kingdom

[*] Corresponding author, a.jaworski@hud.ac.uk

Abstract

Traveling-wave thermoacoustic heat engine is capable of converting heat to acoustic power which in turn can be used to generate electricity by a linear alternator. The thermoacoustic heat engine can work in a wide range of heat quality, giving it the ability to be used for waste heat recovery. In this paper, a new configuration of looped-tube traveling wave thermoacoustic engine is proposed, which consists of two identical stages each having a power extraction point, and the linear alternator connecting these two points working in "push-pull" mode. This enables a more effective acoustic impedance matching compared to the use of multiple linear alternators known in the literature. The laboratory demonstrator has been designed, built and tested. The applied heat source temperature is similar to that of the internal combustion engine exhaust gases in order to explore the potential of using the device for waste heat recovery from road transport. In experiments, the maximum electric power of 48.6 W at thermal-to-electric efficiency of around 6% was achieved with helium at 28 bar as working fluid and 297 K temperature difference across the regenerator. The performance of the device has been analysed and compared to modelling performed using DeltaEC simulation tool.

Keywords: Waste heat recovery, Electricity generator, Thermoacoustics, Multi-stage, Traveling-wave, Push-pull alternator

1. Introduction and literature review

In the last decades, there has been an increasing interest in the utilization of waste heat being released into the environment by a variety of industrial plants as well as road transport vehicles in the form of hot exhaust gases. The serious climate change and global warming encouraged the research towards waste heat recovery because of its potential in reducing consumption of fossil fuels and in relaxing environmental problems. Kim *et al.* (2016) presented the case for waste heat recovery of the internal combustion engine to improve the efficiency, as there is a loss of around 60% of the burnt fuel heat through the exhaust gas and cooling system. Orr *et al.* (2016) reviewed the waste heat recovery of the internal combustion as a method to reduce the CO_2 emission, as converting the waste heat to useful electricity reduces the fuel consumption of cars. Johnson (2002) outlined the technologies to generate cooling power from waste heat of exhaust gases. Thermoacoustic technology has been listed as one of the four vital technologies besides metal hydride cooling, absorption heat pumps and zeolite heat pumps. Later on, Jadhao and Thombare (2013) highlighted the thermoacoustic technology as a direct electricity generation method in his review of internal combustion engine exhaust gas heat recovery.

The common definition of thermoacoustics is the area that deals with the interactions between heat and sound, or in other words the interaction between temperature, density and pressure variations of an acoustic wave. The working principle of thermoacoustic devices is based on a thermoacoustic effect which enables producing sound waves from thermal energy, or vice-versa (Piccolo, 2017). In all of these devices, working fluid is the only moving component and this makes these devices maintenance free and potentially of high longevity. Additionally, they typically use environmentally friendly noble gases as working fluid.

Ceperley (1979) was the first to realize that the phasing between the pressure and velocity of the travelling wave is the same as the phasing of the Stirling engine. Since then travelling wave engines have been designed and built and known as the thermoacoustic Stirling heat engines. Looped tube

thermoacoustic engine is the simplest traveling wave configuration and consists of a long looped resonator (typically one wave length) which contains the regenerator unit and the linear alternator. The first looped tube thermoacoustic engine has been presented by Yazaki *et al.* (1998). It had one wavelength loop and was filled with air. The engine has been designed and built to study the spontaneous gas oscillations in a travelling wave. The low thermal-to-acoustic efficiency (less than 1%) of this engine was discovered to be caused by low acoustic impedance. Kitadani *et al.* (2010) investigated the electricity generation from a looped-tube engine by using a loudspeaker to convert the acoustic power to electricity. The loudspeaker has been placed at the end of a branch. The branch tee has been located at a high sound pressure location which is normally called the "pressure antinode". The engine was found to be able to generate 1.1 W of electricity out of 330 W input heat, leaving the thermal-to-electrical efficiency to be 0.3%.

Yu *et al.* (2009, 2010) proposed the looped tube thermoacoustic electricity generator for remote and rural areas where for economic reasons the working gas was chosen to be air at atmospheric pressure. A blind tube called a "stub" has been introduced to act as a phase adjuster to help the impedance matching between the alternator and thermoacoustic engine. The experimental performance was lower than expected; the engine generated electricity of 5.17 W at a thermal-to-electrical efficiency of 0.65%. Later on, Yu *et al.* (2012) applied some dimensional optimization to the previous design for a better matching between the engine and the loudspeaker. The electricity generated has been doubled to be 11.58 W at a thermal-to-electrical efficiency of 1.65%. Jaworski and Mao (2013) and Abdoulla-Latiwish et al. (2017) demonstrated the practicality of this engine and its suitability to be driven by burning gases instead of electrical heaters. The demonstrator produced 17.8 W of electrical power when the temperature difference across the regenerator reached 340 K. Chen *et al.* (2012) presented a low-cost thermoacoustic engine, constructed to be driven by a propane burner or wood burner. The engine driven by a propane burner consisted of two stages, quarter and three quarter wave length. The experiments showed that the propane burner can generate 15 W of electricity, while the

wood burner was able to generate 12.6 W and 22.7 W at atmospheric and 2 bar mean pressure of air, respectively. The acoustic-to-electric conversion efficiency was concluded to be low due to the low net acoustic power and an inefficient alternator.

Application of multiple self-matching stages has proven to be a solution for the low acoustic impedance of the looped-tube configurations. The name "self-matching" indicates that each stage has an independent power extractor, the device is acoustically symmetric and requires no adjustment or tuning. The first successful attempt has been presented by de Blok (2010, 2012). Four novel engine designs have been built with four identical self-matching stages. The power extraction point of each stage consisted of an independent linear alternator. The four engines of de Blok generated 5.4 W, 18 W, 250 W and 1.64 kW of electrical power.

Yang *et al.* (2014) proposed a thermoacoustic engine with three stages, which has been built later by Li *et al.* (2014).The results of Li *et al.* (2014) proved that the three-stage engine works at high acoustic impedance similar to the four-stage engines. Wu *et al.* (2014) developed the system aimed at generating useful electricity. At mean pressure of 50 bar and the hot side temperature of 650˚C, the engine produced 1.57 kW of electricity by the three alternators at thermal-to-electric efficiency of 16.8%. Bi et al. (2015) improved the engine and pushed the power generation to the highest recorded to date. The mean pressure has been set to 60 bar. The maximum generated electricity was 4.69 kW at 15.6% of thermal-to-electric efficiency and the highest efficiency was 18.4% at generated electricity of 3.46 kW.

Kang *et al.* (2015) constructed a two non-identical-stage engine with one linear alternator placed within the loop line and the other in a branch. This engine used loudspeakers as linear alternators similar to the previous two-stage engines, however, pressurized helium (18 bar) has been used as the working gas. The maximum generated electric power was 204 Watts at 3.41% thermal-to-electric

efficiency and a maximum efficiency of 3.43% was at 183 W electric power.

Current research offers an alternative solution to run a looped tube engine with two self-matching identical-stages coupled with one linear alternator. Each stage is half-wavelength. A potential use of the engine is to recover part of the internal combustion engine exhaust gases and generate useful electricity, as it uses a heat source at the exhaust gases temperature.

2. Conceptual design

The concept of the proposed thermoacoustic engine is shown schematically in **Figure 1**. There are two identical thermoacoustic stages which are distributed within one wavelength loop and generate acoustic power simultaneously. There are also two power extraction points to avoid high acoustic losses in the loop caused by high levels of circulating acoustic power and to allow the stages to self-match. The self-matching stages develop the same acoustic pressure and volume flow rate amplitudes which are out of phase by 180˚. This configuration allows the connection of the linear alternator to two points having the same amplitudes acting out of phase. The idea behind it is to increase the system efficiency by increasing the power output, at a given value of acoustic impedance.

As the thermoacoustic engine was designed to run at temperatures similar to temperatures of exhaust gases from an internal combustion engine, a popular model of a Caterpillar 6.6L engine was chosen as a reference. This is also often used in small marine vessels which is the background of this project. Chalmer (2009) showed that the exhaust gas temperature can reach up to 500˚C. However, it also needs to be considered that the exhaust gases leaving the engine cool down before reaching the exhaust system by a few tens of degrees. Therefore the hot heat exchanger temperature in the thermoacoustic engine was limited to 400˚C in this project. Helium was chosen to be the working gas because it has low Prandtl number and low viscosity which leads to low viscous dissipation. Also, helium has a high speed of sound, which leads to high power density (Swift, 2002). Added to that,

helium has relatively high thermal penetration depth caused by the high thermal conductivity. This is preferred as it allows a relatively large channel width to be used which simplifies the fabrication.

The mean pressure of the thermoacoustic engines is proportional to the power density, and hence, the mean pressure needs to be as high as possible (Swift, 1988). High power density leads to high power generation and efficiency. However, there is a trade-off between the thermoacoustic power density and the fabrication as high pressure requires a lot of fabrication considerations related to pressure vessel design codes. These considerations are associated with the pressure sealing and heat exchanger channel width. Adding to these considerations is the fact that the hot parts of the engine will reach 400˚C, and hence the metal used for construction will have reduced strength. Therefore, the mean pressure used in this project was limited to 28 bar. The linear alternator available for this project was a Q-Drive Model 1S132M, which has an optimum frequency in the range of 50-60 Hz. The linear alternator frequency and the working gas defined the length of the engine. The relatively high speed of sound of the helium and the limited frequency of the linear alternator results in a long wavelength. As will be shown later, the actual length of acoustic path in the device is 16.1 m.

3. DeltaEC simulations

In the current work, DeltaEC package created by the Los Alamos National Laboratory (Ward *et al.*, 2012) was used to simulate the acoustic field in the thermoacoustic device. The calculations are performed by integrating the one-dimensional wave equation at a pre-defined geometry, thermal conditions and working fluid. It integrates the appropriate equations through each of the user-defined elements ("segments"), such as ducts, heat exchangers, compliances, porous media, etc., and ensures that the pressure and volumetric flow rates, both real and imaginary, are matched at the boundaries of the adjacent segments. The integration solves a series of equations of the acoustic pressure (p_1), volumetric velocity (U_1), the mean temperature (T_m) and the total power ($\dot{H}_2$), of the acoustic field through the pre-defined series of segments. The fundamental equations are not repeated here since they were recently reviewed by Abdoulla-Latiwish *et al.* (2017) after Swift (2012). DeltaEC uses the

shooting method to find the guess values consistent with the target results (Ward et al., 2012). As a first step, the boundary conditions were set and the geometries of each component were defined. The solutions were then guessed in order to meet the targets by solving the set of linear thermoacoustic equations.

This section is devoted to the following aspects of DeltaEC modelling. Firstly, the alternator is considered separately in Section 3.1. The push-pull coupling method is illustrated and compared to the compliance housing coupling method. The performance of each coupling method is studied and presented. The engine model is detailed in section 3.2. This section shows the engine layout, model boundary conditions and simulation results. Finally, a sensitivity study of the thermoacoustic engine performance to the geometrical parameters of selected parts is presented in section 3.3.

3.1. Linear alternator simulation

Figure 2 shows the linear alternator configuration of the push-pull and compliance coupling. In the push-pull coupling, acoustic power flows from both sides of the housing, pressure oscillations acting out of phase on the linear alternator piston, while for the compliance coupling there is an active acoustic power input from one side and a dead volume acting as an acoustic compliance on the other. At a specific loop acoustic impedance and phase difference, the push-pull coupling is expected to generate twice the electricity compared to the compliance housing coupling. This is because the acoustic impedance seen by the linear alternator is the algebraic sum of the identical local acoustic impedances at two corresponding points in the engine loop. For the compliance coupling, the local acoustic impedance would only act on one side of the linear alternator.

A series of simulations was undertaken to investigate the linear alternator performance for both the push-pull and compliance housing coupling at various acoustic impedances and phase differences (between volume flow rate and the pressure) at a specific frequency and stroke. The performance was represented by the electricity generated and the acoustic-to-electrical efficiency. The acoustic

impedance is defined as the ratio of pressure to volume flow rate ($Z = p_1/U_1$) (Swift, 2002). Here the performance was studied for a range of frequencies 50-60 Hz, while the peak-to-peak stroke was held constant at 12 mm for the sake of comparisons. However, the constant stroke and frequency lead subsequently to constant velocity amplitude:

$$U_1 = \omega A \xi \tag{1}$$

where ω is the angular frequency, A is the piston cross-section and ξ is the piston displacement. This means that the simulations consider the change in the acoustic impedance in response to the change in pressure amplitude. In push-pull coupling, the active pressure acting on the linear alternator is the algebraic sum of the pressure amplitudes on both sides, while in the compliance housing the active pressure acts only on one side. Hence, at a given acoustic impedance and phase difference, the push-pull coupling is expected to generate double the electricity as compared with the compliance housing coupling, as the acoustic power is:

$$E = \frac{1}{2}|p_1||U_1|\cos\Phi_{pU} \tag{2}$$

where Φ_{pU} is the phase angle between the volume flow rate phase and the pressure phase.

The DeltaEC model consists of a linear alternator segment with mathematical calculation segments to apply an oscillatory flow. The simulation considers that the acoustic impedance seen by the linear alternator piston is the impedance of the loop. The push-pull model has two equal and out of phase acoustic impedances acting on the piston from both sides, while the compliance model has only one side excited and a compliance from the other side which represents the gas volume between the alternator body and the housing. For the sake of comparisons, the compliance volume was taken as 2.5 litres to replicate the physical alternator body. The gas volume has been calculated based on the volume of standard 6 inch pipe minus the actual physical volume of the linear alternator. As the study focuses on the local acoustic impedance, the phase difference (Φ_{Up}) is the difference between

volumetric flow phase and pressure phase ($Ph(U) - Ph(P)$). This is the case for both configurations since pressure "across" the piston for push-pull arrangement is in essence $2 \times P$.

The linear alternator specifications listed in **Table 1** were used as input values to a DeltaEC simulation model. Higher oscillation frequency leads to higher power output from the linear alternator, however, the alternator efficiency is higher at lower frequency. A frequency of 56 Hz has been selected for this study as a trade-off between the power and efficiency, and because it is close to the optimum frequency of the thermoacoustic engine (as will be presented later). **Figure 3** presents the performance graphs: generated power and efficiency are plotted as a function of phase difference between velocity and pressure, with local acoustic impedance as a parameter. The simulation results confirm that the push-pull configuration requires approximately half the loop acoustic impedance required by the compliance housing to generate the same electrical power. On the other hand, comparing the linear alternator performance at a given value of loop acoustic impedance for the push-pull configuration (e.g. 3.8 MPa·s/m^3 in Figure 3a) to the linear alternator performance at double the local acoustic impedance for the compliance housing configuration (e.g. 7.6 MPa·s/m^3 in Figure 3b), the compliance configuration was able to generate slightly higher power than the push-pull configuration (by approximately 2 - 4%). This increment was caused by the linear alternator as it ran at a higher efficiency at higher local acoustic impedance.

Such analysis is generally useful in designing the thermoacoustic network and deciding the coupling location, and in particular the required local acoustic impedance and phase difference at the coupling location. For a specific electrical power and efficiency, a range of acoustic impedances can be selected. The selection of the local phase difference can determine the exact amount of local acoustic impedance. Alternatively, the graphs can be used during the modelling and optimization. Optimizing any part of the acoustic network will have an influence on the acoustic impedance and phase difference along the engine. These graphs help to track the influence on the performance of the

alternator.

3.2. Thermoacoustic engine model

The thermoacoustic engine usually consists of a thermoacoustic core – which contains the ambient heat exchanger (AHX), regenerator (REG), hot heat exchanger (HHX), thermal buffer tube (TBT) and the secondary ambient heat exchanger (2nd AHX) – and an acoustic resonator which consists of the pipes connecting the core and linear alternator. The proposed design has two stages; however, these are geometrically identical. Therefore, DeltaEC model considers only one stage, i.e. one "half" of the configuration to reflect its symmetry and also to simplify the solution process, as illustrated by a block diagram in **Figure 4**. Two self-excited hypothetical flows at two different locations have been considered to represent the second stage. The first self-excited hypothetical flow is introduced at X=0 (cf. **Figure 4**) to provide the necessary coupling between stages. The second self-excited hypothetical flow is applied to the side of the linear alternator connected to the second stage (cf. point B).

The boundary conditions of the first self-excited hypothetical flow were set in the following manner: the temperature, pressure amplitude, volumetric flow rate and total power were set to be equal at the beginning and the end of the simulated stage (at X=0 and X=λ/2): $T_{m,X=0} = T_{m,\mathrm{X}=\lambda/2}$; $|p_{1,\mathrm{X}=0}| = |p_{1,\mathrm{X}=\lambda/2}|$; $|U_{1,\mathrm{X}=0}| = |U_{1,\mathrm{X}=\lambda/2}|$; $\dot{H}_{2,\mathrm{X}=0} = \dot{H}_{2,\mathrm{X}=\lambda/2}$, (using the already defined symbols). In line with the physics explained above, the phases of pressure and velocity were set to be shifted by 180°° at the end of the stage with reference to the beginning (at X=0 and X=λ/2): $Ph(p_1)_{\mathrm{X}=0} = Ph(p_1)_{\mathrm{X}=\lambda/2} + 180°$; $Ph(U_1)_{\mathrm{X}=0} = Ph(U_1)_{\mathrm{X}=\lambda/2} + 180°$, where symbol "$Ph(\,)$" denotes phase angle of a quantity in brackets.

The boundary conditions of the second self-excited hypothetical flow were set based on the physics of push-pull operation. The volumetric velocity and its phase were kept equal on both sides of the alternator piston. The pressure amplitude was set to be equal on both sides, but the phase was set "out

of phase", i.e. phase difference of 180°:$|p_{1,\mathrm{A}}| = |p_{1,\mathrm{B}}|$; $Ph(p_{1,A}) = Ph(p_{1,B}) + 180°$. This results in $\dot{E}_{2,A} = -\dot{E}_{2,B}$, which means that acoustic power flows to the alternator from both directions to be converted to electricity. Similarly, $\dot{H}_{2,\mathrm{A}} = -\dot{H}_{2,\mathrm{B}}$. The boundary conditions were set as targets at locations A and B (cf. Figure 4)

The DeltaEC simulation considered several operational and performance parameters. The full process of optimization is omitted here for brevity. The following results and discussion are based on the optimized model. The results of one stage (half wavelength) are replicated over the other stage to present the results over the full engine length. Table 2 shows the investigated ranges of parameters during the optimisation and the optimum values of the main geometries of the engine parts.

Figure 5 shows the simulation results. The graphs on the right are magnified areas marked by green dashed lines of the graphs on the left. **Figure 5a** shows the calculated pressure amplitude distribution along the engine loop. There are two peaks, both are near the regenerators of the two stages. There is a major pressure drop at the regenerator caused by the flow resistance. **Figure 5b** shows the distribution of volumetric velocity along the thermoacoustic engine. The engine has been designed to have the lowest volumetric flow rate at the regenerator to minimize the viscous dissipation. The effect of the temperature difference across the regenerator is clearly seen in the volumetric flow rate profile as it increases within the regenerator length from the cold end towards the hot end. There is a volumetric flow rate drop at the linear alternator branch caused by the power extraction at the linear alternator.

Figure 5c is the local acoustic impedance profile along the engine. It can be seen that the local acoustic impedance is nearly maximum at the regenerators which is one of the design strategies. It then drops within the regenerator length, which is caused by the pressure drop and velocity amplification. The impedance drops until the middle of the feedback loop and increases again which

corresponds to the changes of the pressure and volumetric flow rate. **Figure 5d** shows the phase difference between the velocity and pressure oscillation along the engine. This graph illustrates that the phase difference at the regenerator is much higher than travelling wave phasing, which could not be avoided at the design stage.

Figure 5d shows that the phase difference shifts with 90° in short distance between the regenerator and the linear alternator. This means that setting the phase difference at the regenerator to be zero shifts the phase difference at the linear alternator to about -90°. **Figure 3a** shows that the linear alternator cannot generate electricity at this phase difference. The choice of phase difference is a trade-off between acoustic power generation at the regenerator and electricity generated by the linear alternator. **Figure 5e** shows the acoustic power distribution along the engine. It is shown that 86.8 W is fed into the ambient end of the regenerator and it is amplified to 155.2 W at the hot end. The alternator extracts 39.8 W of acoustic power (from each side) based on the baseline model. The numerical results show that the engine runs at a frequency of 55.1 Hz at optimized dimensions (shown later in **Table 3**). The regenerator temperature difference is 320 K and the piston peak-to-peak displacement is 6 mm (as these are the values obtained experimentally, see Section 6). Theoretically, engine generates 79.5 W of electricity at an optimum load resistance of 10 Ω.

3.3. Sensitivity analysis

The optimum geometries of the system components were obtained from the DeltaEC optimisation process. Having completed the optimisation procedure, it is also worth conducting the sensitivity analysis in order to show the influence of selected dimensions on the electricity generated by the engine. Some of the results of such analysis are shown in **Figure 6**. The data is presented using dimensionless geometry which relies on normalisation by the selected dimension. The optimal geometry ratio equals unity at the maximum generated electricity of 79.5 W.

As shown in **Table 2**, the optimum ratio of the core to feedback loop area is 6 and the optimum core and feedback loop diameters are 102.2 mm and 40.8 mm, respectively. For the purpose of this sensitivity analysis, only one of the dimensions will be varied while the other kept constant. The optimization showed that the optimum core diameter is 104 mm over a range of 75–125 mm. The core diameter sensitivity curve shown in **Figure 6a** is non-symmetric around 1 as the core diameter of 102.2 mm is selected to match the internal diameter of 4 inch for standard tubes and fittings. Starting from the minimum, the increase of the core diameter leads to the increase of the local acoustic impedance as it increases the local pressure and reduces the local velocity. High acoustic impedance is favourable as it increases the acoustic impedance along the engine. The increase of the core diameter increases the phase difference at the regenerator. At a certain value of diameter, a further increase of the core diameter increases the phase difference at the regenerator to become higher than the current phasing and leads to a decrease in the generated acoustic power by the regenerator, which reduces the engine performance.

The feedback diameter is the most sensitive parameter with the optimum value of 40.8 mm. The sensitivity curve is almost symmetrical around 1 as shown in **Figure 6a**. Decreasing the feedback loop diameter leads to an increase in the acoustic impedance along the engine. However, it shifts the alternator phase difference to the far left end of **Figure 3a**, which reduces the electricity generation. On the other hand, an increase in the feedback loop diameter reduces the acoustic impedance and hence reduces the alternator performance.

Prior to optimizing the regenerator length, its hydraulic radius must be optimized. The hydraulic radius is the ratio of gas volume to gas-solid contact area, but for a wire mesh screen geometry can be simplified to (Ward *et al.*, 2002):

$$r_h \cong d_{wire} \frac{\phi}{4(1-\phi)} \tag{3}$$

where

$$\phi \cong 1 - \frac{\pi m d_{wire}}{4} \tag{4}$$

Here d_{wire} is the mesh wire diameter, m is the mesh count and ϕ is the porosity. Swift (2002) summarizes the relationships between the hydraulic radius and the thermal and viscous penetration depths in the regenerator as $\delta_v \gg r_h$ and $\delta_k \gg r_h$. Yu et al. (2005) concluded that the optimum ratio of the hydraulic radius r_h to the thermal penetration depth δ_k for travelling wave engines is between 4 and 7. From the optimization, it has been concluded that the ratio needs to be 5.1 in the middle of the regenerator. **Figure 6b** shows the sensitivity curve of δ_k/r_h at the centre of the regenerator. Increasing the regenerator length increases the acoustic impedance as well as the flow resistance. The optimized regenerator length was 73 mm. It is a very sensitive parameter with the curve peaking at 1. At regenerator length values higher than the optimum, the flow resistance reduces the performance of the engine, as also illustrated in **Figure 6b**. Reducing the regenerator lengths below the optimum decreases the engine performance as it will run at lower acoustic impedance.

The hot heat exchangers are of parallel-plate type. Their optimization includes the plate spacing and porosity (which in DeltaEC then defines plate thickness). The optimization of any of these two parameters will consider the other at the optimum. They were studied for all the three heat exchangers; however, the results of the HHX are presented here as representative. The engine performs better at low fin spacing or high porosity as this leads to higher gas-to-metal contact area. The final values of 1 mm and 34.4 % were the lowest fin spacing and highest porosity, respectively, which could be achieved using available manufacturing methods. The sensitivity curves of **Figure 6c** consider these two values as optima. The practical built of heat exchangers is the classic cross-flow parallel-plate heat exchanger as will be discussed in Section 4.1. The thermal buffer tube reduces the cross sectional area to suppress Rayleigh streaming, as recommended by Swift (2000). The optimum length of the TBT is 162 mm, and it is not a very sensitive parameter as shown in **Figure 6c**.

4. Experimental apparatus

The schematic of the experimental apparatus is shown in **Figure 7**. Its main components include two thermoacoustic core sections, the casing containing the alternator and the necessary acoustic network (two "halves" of the resonator loop and connections to the two ends of the alternator casing). The detailed design had to incorporate a number of requirements, mainly including: (i) the need to easily assemble and disassemble parts of the apparatus in the research environment in order to insert or replace the subcomponents and embedded sensors; (ii) the need to meet the necessary safety standards which required the use of certified subcomponents wherever possible, including the correct grade of materials from the temperature point of view. The main parts of the apparatus will be described in the subsections below.

4.1. Thermoacoustic cores

As noted in section 3.2., thermoacoustic cores consist of AHX, REG, HHX, TBT and 2ndAHX. **Figure 8a** shows a cross-sectional view of the assembly. The regenerator and the adjacent heat exchangers are 102.2 mm (4 inch) in diameter. The diameter of this section then reduces towards 2ndAHX to 77.9mm (3 inch) along a conical TBT. To reduce the gas leakage problems which might appear at elevated temperatures when sealing the thermoacoustic cores, the regenerator holder, HHX, TBT and the flanges on two ends were fabricated in one piece.

4.1.1. Hot heat exchanger

The HHX was manufactured from low carbon steel. The choice of material is a trade-off between the thermal conductivity and the material mechanical properties at elevated temperatures. It has a 102.2 mm (4 inch) circular face diameter and 40 mm length in the direction of the flow oscillation. The photograph in **Figure 8b** shows the overall view as well as a more detailed fragment of the layout of helium channels. The "ports" to the side of the HHX are used to insert the electrical cartridge heaters. Up to six pairs of 100 W cartridge heaters, WATLOW FIREROD 1/8 inch diameter, can be

introduced into each HHX.

The channels on helium side had a “comb-like” shape and were cut out using Electrical Discharge Machining (EDM) to form channels of 1 mm width, and fins of 7 mm in length and 0.5 mm in width The total contact area between the fins and the gas is 0.149 m^2 which, based on calculations, could allow the HHX to transfer more than 850 W of heat to the helium. The porosity on helium side is 34.4%. The design gas oscillation peak-to-peak displacement is 13.5 mm. The length of the heat exchangers is about three times the displacement to have enough length to accommodate the heaters. The heat exchanger was designed for pressure endurance using SolidWorks: the minimum safety factor was around 15 at 400˚C and around 5 at 500˚C (note that the rig is aimed to run at 400˚C).

The HHX had two circular sleeves projecting 30 mm in length from each side. The regenerator holder and TBT were welded to these two low carbon steel sleeves to ensure that the thermal stresses caused by the welding would not bend the very fine fins. A 4 inch diameter tube with 45 mm length is welded to the top sleeve – forming the regenerator “can” which in turn is welded to a 300 lb 4 inch flange. The bottom sleeve was welded to a conical section, with 102 mm length, which further had a straight 3 inch diameter, 30 mm long, sleeve and a 300 lb 3 inch flange welded at the bottom. The overall length of the TBT created in this way is 162 mm (the optimum as given in section 3.3).

4.1.2. Regenerator

Figure 9 shows the assembly process for the regenerator. Its total length is 73 mm, made of 445 stainless steel mesh screen disks with 102 mm diameter. The diameter of the mesh wire is 65 μm and the aperture is 180 μm. The number of stacked mesh screens is about 88% of the calculated/expected number. **Figure 9a** shows a single screen on a coarse diamond mesh acting as a spacer (1.3 mm thickness). **Figure 9b** shows a half-filled regenerator with a tight clearance with the wall of the “can” visible. A thermocouple embedded in the regenerator can also be seen. **Figure 9c** shows the

completed regenerator with another coarse mesh spacer on top. To ensure that the regenerator has a uniform number of screens per unit length, a uniform amount of force was applied by a cylindrical "stamp" after inserting each pair of disks during the process. The hydraulic radius is 60.5 μm and the volume porosity is 78.9%. The regenerator holder was machined to have an inner diameter of 102.2mm. The small clearance between the holder and regenerator screens is to avoid "bridging" the oscillatory flow around the regenerator, which could encourage streaming and heat transfer without generating acoustic power.

4.1.3. Ambient Heat Exchangers

The AHX shown in **Figure 8c** is a cross flow heat exchanger where helium oscillates in the small channels perpendicular to the circular face (101.75 mm diameter), while water flows through the cross flow channels that can be seen on the side. The circular face has 1 mm step proud of the block surface for alignment with the regenerator holder flange from one side and the reducer flange from the other. The AHX is made out of a block of copper to ensure good heat transfer from the helium to the water side. It has a length of 30 mm. On both the water and helium sides, continuous channels were cut out using EDM to form "square wave" channels leaving fins in an "inter-digitated" staggered pattern. The roots of the fins are adjacent to a cooling water channel. The fins are 0.5 mm wide. Their length is 9 mm on the helium and 6 mm on the water side. The channels between fins are 1 mm wide. The contact area between the helium and the heat exchanger channel walls is 0.1317 m^2, and 0.1054 m^2 between the cooling water and channel walls. The AHX was designed to have a higher contact area from the helium side as the helium has a lower heat transfer coefficient, as well to increase the porosity on the helium side. These two areas were used in the conduction-convection heat transfer calculations which showed that AHX can transfer more than 600 W of heat from the helium to the water side at a temperature difference of 4˚C only. At the design oscillation amplitude, the peak-to-peak displacement is 14.8 mm. The AHX length is roughly twice the displacement for the ease of fabrication. The porosity of AHX is 31.2%. The heat exchanger design was modelled for pressure

loads using SolidWorks which predicted the minimum safety factor of about 10.

The 2nd AHX is similar to the AHX with slightly smaller dimensions, as the aim of this part was to avoid heat leaks beyond the thermoacoustic core. Like AHX, it was manufactured out of a block of copper and its cross-flow principle of operation is the same. The circular face is 77.4 mm in diameter, while the length is 20 mm which is approximately equal to the design peak-to-peak amplitude of 19.5 mm. The contact area between the helium and the heat exchanger channel walls is 0.056 m^2, and 0.018 m^2 between the cooling water and channel walls. The calculations showed 2nd AHX can transfer over 400 W of heat from the helium to the water at a temperature difference of 3˚C only. The simulation of the pressure endurance using SolidWorks gave the minimum factor of safety of 12.3. The cooling water was pumped through AHX and 2nd AHX of both stages; the details of the cooling system operation were already given by Hamood (2016).

4.2. Acoustic network

The acoustic network comprises of the pipework and fittings connecting the thermoacoustic cores to the linear alternator (cf. **Figure 7**). All these are schedule 40 stainless steel welded pipes. The main purpose of the feedback loop is to deliver acoustic power from the end of a stage to the beginning of the other at a convenient acoustic phasing. The acoustic network starts with a 3 to 1½ inch standard reducer connecting the secondary ambient heat exchanger of one of the cores to the 1½ inch pipe. Because of the large volume of the linear alternator housing and the width of the 3 inch flange, a 100 mm long tube, 1½ inch in diameter is welded after the reducer. This is welded to an equal tee junction connecting the main feedback branch to a trunk connected to the linear alternator housing. Following the alternator branch, a 1½ inch tube was welded to the tee at a total length of 6880 mm. This was divided into five pieces connected by long radius elbows. The last piece of the 1½ inch feedback tube is connected to a standard reducer 1½ to 1 inch, followed by a standard 1 inch tube of 275 mm length. The short piece of the reduced diameter essentially acts as an inertance to correct the phase between

pressure and velocity as indicated by DeltaEC simulations. The last piece of the feedback branch is a standard 1 inch to 4 inch transition piece to fit the 4 inch diameter of the AHX of the other thermoacoustic core.

4.3. Linear alternator and its casing

The linear alternator housing shown in **Figure 10** was placed between the two branches of the two stages. The main body was made out of 6 inch pipe of 175 mm length, with appropriate 6 inch flanges to connect to the acoustic network. The total length of the alternator housing is 616.6 mm, which is the distance between the centres of the loops. The alternator model used in this research has an asymmetric build designed for use with compliance coupling – the front side of the piston being a plain circular surface, while the back side is exposed to a dead volume occupied by suspension, magnets and coils. To overcome this asymmetry, two design decisions were made. Firstly, the piston was positioned in the middle of the trunk in between the two feedback loop branches to ensure an out of phase acoustic power is applied to the sides of the piston. Secondly, PVC inserts (cf. **Figure 10b**) were placed in the cavity to reduce the effect of gas volume, which would normally act as an acoustic compliance leading to a change in the pressure amplitude and phase. Based on a rough estimation of the volume of the linear alternator body, the plastic insert was fabricated to fill the cavity between the alternator and the housing, leaving an approximate volume equivalent to the 1½ inch tube to match the actual pipe present on the other side of the piston. A glass-to-metal wire feedthrough was used to pass the alternator wires through the linear alternator housing vessel (cf. Figure 10a).

4.4. Summary of engine layout

Figure 11 shows a photograph of the build of the experimental rig in the laboratory after connecting all the parts together. Thermoacoustic cores are wrapped with insulation blankets to reduce heat losses. Water lines (red hoses) connect the AHXs to the water cooling system. Data acquisition PC

with associated instrumentation is placed in the rig's vicinity. In addition, Table 3shows a list of the parts of the thermoacoustic core, acoustic network and linear alternator housing.

5. Instrumentation and measurement

The temperatures within selected components of the rig were monitored using 21 thermocouples (Type K, TC-Direct models 405-010 and 405-011). Twelve thermocouples were used to monitor the thermoacoustic cores (six per stage – cf. **Figure 8a**) – three were located in the middle of each heat exchanger (AHC, HHX, 2ndAHX) channel and three along the regenerator: two ends and the middle (cf. **Figure 9b**). The thermocouples at the ends of the regenerator were placed at the spacers. To pass the thermocouples to the middle of the regenerator, half of the regenerator screens were punched with 1 mm diameter holes and eight were line cut in the middle, as shown in **Figures 9a** and **9b**. Multiple feedthrough assemblies (TC-Direct model 941-339) were used to pass the thermocouple leads to the engine – cf. TC feedthrough 1 and 2 in **Figure 8a**.The linear alternator temperature was monitored by a thermocouple attached to its body to prevent accidental overheating and damage to the coils. Eight additional thermocouples were installed in the cooling system; one at the cooling water inlet and one at the outlet of each of the four AHXs. All thermocouples were connected to a data acquisition card, OMEGA OMB-Daq Temp Model 7 controlled by a LabVIEW programme used to save the measured values to the PC.

Overall, the rig was equipped with 19 ports to install the pressure sensors (high pressure microphones) as shown schematically in **Figure 12**. Their location counting from the AHX of first stage (cf. Figure 4) were X_1=670 mm, X_2=1640 mm, X_3=2400 mm, X_4=3870 mm, X_5=4280 mm, X_6=5280 mm, X_7=6280 mm, X_8=7900 mm, X_9=8720 mm, X_{10}=9690 mm, X_{11}=10450 mm, X_{12}=11920 mm, X_{13}=12330 mm, X_{14}=13330 mm, X_{15}=14330 mm and X_{16}=15950 mm, while three transducers numbered PT17, 18 and 19 were placed in the alternator housing branch. Seven pressure sensors, PCB PIEZOTRONICS model 112A22, were installed at different positions along the loop. All

pressure transducers have a resolution of 7 Pa, and were used to measure the pressure amplitude, phase angle and frequency. Clearly, not all 19 ports could be instrumented at the same time, but certain characteristic locations were chosen after preliminary tests. These locations were X_1, X_2, X_6, X_7, X_9, X_{10} and X_{17}. The unused ports were closed with blanking plugs. The pressure transducers are connected to the same data acquisition card and LabVIEW programme. The phase difference between any two sensors could be recorded. A signal conditioner, PCB PIEZOTRONICS model 480B21, was connected between the sensors and the data acquisition card. Acoustic power flow was measured between selected pairs of sensors using "two-microphone method" (Fusco *et al.*, 1992):

$$W_{2mic} = \frac{A}{2\rho_m a \sin(\omega\Delta x/a)}\left(Im\,[p_1\widehat{p_2}]\left\{1-\frac{\delta_v}{4r_h}\left[1-\frac{\gamma-1}{\sqrt{\sigma}}+\left(1+\frac{\gamma-1}{\sqrt{\sigma}}\right)\frac{\omega\Delta x}{a}\cot\left(\frac{\omega\Delta x}{a}\right)\right]\right\}\right.$$
$$\left.+\frac{\delta_v}{8r_h}(p_1^2-p_2^2)\left[1-\frac{\gamma-1}{\sqrt{\sigma}}+\left(1+\frac{\gamma-1}{\sqrt{\sigma}}\right)\frac{\omega\Delta x}{a}\csc\left(\frac{\omega\Delta x}{a}\right)\right]\right) \quad (5)$$

Here, $[p_1\widehat{p_2}] = p_1 p_2 \sin\alpha$, where p_1 and p_2 are the pressure amplitudes at the two specific locations and α is the phase difference between the sensors. Δx is the distance between the two sensors in the oscillation direction, ω is the angular frequency, ρ_m is the gas density, γ is specific heat ratio, σ Prandtl number and δ_v is the viscous penetration depth. The phase difference between the pressure sensor PT17 and the piston displacement needs to be recorded to calculate the acoustic power at the piston by the general acoustic power equation (2), having obtained the volumetric flow rate from equation (1) using the measured value of the piston displacement and the frequency. Then the acoustic power can be calculated using pressure amplitude of PT17, the calculated volume flow rate and the phase difference between the pressure and the piston displacement (velocity and displacement are shifted by 90° and this needs to be accounted for in the calculation).

The acoustic power entering and leaving the core was calculating using two-microphone method applied between locations X_6 and X_7 and between locations X_9 and X_{10}, respectively. The acoustic power at the piston was calculated by the piston displacement and the pressure at locations (e.g. PT17-

piston). The net generated acoustic power is considered to be the power at the piston plus the power entering the feedback loop minus the power entering the core. Clearly, the calculated net power is less than the real value as the power entering the thermoacoustic core is measured about 2.5 m before the core and the power entering the feedback loop is measured about 1.2 m after the core, and there is an acoustic power loss in the tubes and fittings, tee connections and the linear alternator housing and connectors.

The piston displacement was measured by a laser displacement sensor (KEYENCE, model LK-G152). A high pressure sight glass window (VISILUME toughened line glass type 64), was installed to enable such measurements as shown in **Figure 10a**. The electrical power generated by the linear alternator was calculated by multiplying the measured voltage and current. The voltage and current were measured by digital multi-meters (Fluke 28II digital multi-meter; current accuracy ±0.2%; voltage accuracy ±0.1%).

The cartridge heaters used to simulate the thermal input to the engine were connected to two 0-900 W electrical autotransformers to control the heating power of the heat exchanger by controlling the voltage. The electricity consumed by the heaters was measured by an inline power meter and was considered to be the heating power of these heaters. The linear alternator was connected to a variable load resistance box to dissipate the generated electricity. The box has three knobs to vary the resistance value from 0-100 Ω.

6. Results and discussion

The engine has been tested using helium as working gas at 28 bar for a range of load resistance values. The weak oscillation started when the helium at the regenerator hot side reached a temperature of approximately 230˚C and the temperature difference was about 185 K. It usually takes less than 20 minutes to reach that temperature difference. The test data were recorded when the engine

performance data became stable. During the experiments, the temperature distribution along the thermoacoustic core and the pressure distribution along the engine were recorded. A verification of the simulated pressure amplitudes and acoustic power distribution is presented in this section. The performance of the engine at different load resistance values is presented and compared to the simulation.

6.1. Pressure and temperature measurements

The pressure amplitude distribution has been measured in all the sixteen locations. Additionally, the simultaneous measurement of pressure signals and phase difference between each pair of adjacent transducers allows calculating the acoustic power at the midpoint between adjacent transducers using Equation (5). The engine runs at a frequency of 54.68. As shown in **Figure 5a**, the distribution of the pressure amplitude along the engine shows a good match between the experimental and the theoretical results. There are small differences, however, between the pressure amplitudes at corresponding points for the two stages. This is considered to be related to the construction of the linear alternator described in Section 4.3, which results in a mild asymmetry in the whole loop configuration. All the left hand side (LHS) points have slightly higher amplitudes than the right hand side (RHS) points. The phase differences between pairs of pressure signal from corresponding points also reflect some degree of asymmetry. In practice, the phase differences can be as much as 194˚, compared to the theoretical 180˚ phase difference. In addition, Figure 5e compares the experimental acoustic power to the simulation results. Generally, the trends of two results are in agreement, while there is a 20-30% discrepancy in absolute power levels. A possible reason of the discrepancy is that the engine parts geometries as built do not fully match the simulation geometries.

6.2. Engine performance at different load resistance values

Resistive load has been applied on the linear alternator to measure and dissipate the obtained electric power. The value of the load resistance will affect both the electrical part of the alternator and the

acoustic field of the thermoacoustic engine. In this investigation, the load resistance on the linear alternator has been varied, while the heat input to the engine has been kept at a constant flux. For the linear alternator alone, at the design operating frequency, increasing the load resistance will normally lead to an increased acoustic impedance imposed by the linear alternator to the oscillatory flow into the branch. As a result, the acoustic pressure in the branch, and the acoustic pressure difference on the alternator as well, increase in amplitude. The piston displacement increases slightly too, so that the linear alternator and the branch act more like a standing wave resonator that will draw less power from the engine loop. When such an alternator is connected to the engine loop as is the case in this work, this results in an acoustic pressure in the engine loop of a higher amplitude.

Figure 13a shows the net acoustic power generated in one stage, the acoustic power delivered to one side of the linear alternator and the piston displacement from the experimental measurements when different load resistances were applied. The load resistance was varied in the range of 26.3 – 92.5 Ω. It clearly indicates that the loop engine favours an acoustic condition of a slightly higher acoustic impedance, so more acoustic power could be generated from a constant heat input to the engine. Any load less than 26.3 Ω damps the oscillation and eventually stops the engine. **Figure 13b** shows the electricity output measured from the load resistance connected to the linear alternator and the predicted values using DeltaEC model. The experimental results are indicated by the symbols, and the line shows the prediction. The circles represent the average of four experimental readings and the error bar their variations. The load resistance, the acoustic pressure amplitude at the linear alternator and the temperature difference across the regenerator measured were applied as the boundary conditions to the DeltaEC model. A maximum electrical power of 48.6 W was generated when the load resistance is 30.8 Ω. With a further increase of the load resistance the electricity output gradually reduces.

The electrical power output is a combined result of the acoustic power delivered to the alternator and the transduction efficiency of the alternator. It is known that, the transduction efficiency peaks when the load resistance is equivalent to the coil resistance of the alternator (Yu et al 2009), which is 2 ohm (Table 1). The electrical power output is also proportional to the square of the piston displacement, which increases continuously as seen in **Figure 13a**. The decreasing transduction (acoustic-to-electric) efficiency when the load resistance increases is shown in **Figure 14**. It reduces from 53% to nearly 20%. Also shown is the thermal-to-electric efficiency of the engine combined with the linear alternator. At a load resistance of 30.8 Ω, the thermal-to-electric efficiency reaches a maximum of 5.5%, This coincides with the maximal electrical power mainly due to the higher acoustic power delivered by the engine as discussed.

Figure 15a shows the temperature difference measured across the regenerator at various load resistances. At the same heat flux input to the engine, the temperature difference on the regenerator reduces gradually with the load resistance, as a result of enhanced heat transportation due to high volume flow rate. The acoustic power generated, however, increases as shown in **Figure 13a**. At the load resistance of 30.8 Ω, the temperature difference across the regenerator is 297 K. The temperature distribution along the thermodynamic section is shown in **Figure 15b**. It can be seen that there is a significant reduction in the temperature at the hot heat exchanger, the hot side of the regenerator and the middle of the regenerator when the load resistance increases its value. The non-linear temperature distributions are considered to be caused by Gedeon streaming, which is one type of mass streaming flows occurring in acoustic resonators. Also shown in the figure is the linear distribution of the temperature measured in the regenerator, when there was no acoustic oscillation. This clearly indicates that the nonlinear temperature distribution is highly connected to the acoustic oscillation and its further effects. The experiment further illustrates that the nonlinear temperature distribution became more significant when a higher load resistance was applied.

7. Conclusions

A new configuration of a two-stage traveling wave thermoacoustic engine has been constructed and tested. A thermoacoustic engine utilizing one linear alternator in a “push-pull” mode to extract acoustic power from both stages, has been proposed as a solution for the low acoustic impedance of the looped tube. Simulations were undertaken to compare the linear alternator performance for the push-pull and compliance housing coupling at various acoustic impedances and phase differences. The engine DeltaEC model considered only one stage by utilizing the existing symmetry between the two stages. The sensitivity analysis to characteristic engine dimensions showed that the core and feedback diameters are the most sensitive parameters. The experimental investigation has shown that the device constructed could deliver the maximum electric power of 48.6 W at a thermal-to-electric efficiency of 5.5% with helium at 28 bar as working medium and at 297 K temperature difference across the regenerator.

Acknowledgment

Ahmed Hamood would like to acknowledge the Human Capacity Development Program (HCDP) sponsored by Kurdistan regional government. Artur J. Jaworski would like to acknowledge funding from the Royal Society Industry Fellowship scheme (grant IF110094, 2012-2015). All authors acknowledge InnovateUK for funding under TITAN project (ref no. 131497). A loan of necessary alternators, laser displacement sensors and resistance boxes from colleagues in EEE, University of Manchester, is gratefully acknowledged.

References

Abdoulla-Latiwish, K.O.A, Mao X. and Jaworski A.J., 2017. Thermoacoustic micro-electricity generator for rural dwellings in developing countries driven by waste heat from cooking activities, Energy, Vol 134, pp. 1107-1120

Bi, T., Wu, Z., Zhang, L., Yu, G., Luo, E. and Dai, W., 2015. Development of a 5kW traveling-wave thermoacoustic electric generator. *Applied Energy*.

Chalmers A., 2009. Engine Horse Power and Exhaust Flow. Available: http://www.asia.donaldson.com/en/exhaust/support/datalibrary/1053747.pdf.

de Blok, K., 2010. Novel 4-stage traveling wave thermoacoustic power generator. In *ASME 2010 3rd Joint US-European Fluids Engineering Summer Meeting collocated with 8th International*

Conference on Nanochannels, Microchannels, and Minichannels (pp. 73-79). American Society of Mechanical Engineers.

de Blok, K. and Systemen, A.T., 2012. Multi-stage traveling wave thermoacoustics in practice. In *19th International Congress on Sound and Vibration, Vilnius*.

Ceperley, P.H., 1985. Gain and efficiency of a short traveling wave heat engine. *The Journal of the Acoustical Society of America*, *77*(3), pp.1239-1244.

Chen, B., Yousif, A.A., Riley, P.H. and Hann, D.B., 2012. Development and assessment of thermoacoustic generators operating by waste heat from cooking stove. *Engineering* Vol.4 No.12, Article ID:25859,4 pages

Fusco, A.M., Ward, W.C. and Swift, G.W., 1992. Two-sensor power measurements in lossy ducts. *The Journal of the Acoustical Society of America*, *91*(4), pp.2229-2235.

Hamood, A.M., 2016. Two-stage thermoacoustic electricity generator with push-pull linear alternator. PhD Thesis, University of Leeds, Leeds, UK

Jadhao, J.S. and Thombare, D.G., 2013. Review on exhaust gas heat recovery for IC engine. *International Journal of Engineering and Innovative Technology (IJEIT)*, *2*(12).

Johnson, V.H., 2002. *Heat-generated cooling opportunities in vehicles* (No. 2002-01-1969). SAE Technical Paper.

Jaworski, Artur J., and Xiaoan Mao, 2013. "Development of thermoacoustic devices for power generation and refrigeration." *Proceedings of the Institution of Mechanical Engineers, Part A: Journal of Power and Energy*: 0957650913493622.

Kang, H., Cheng, P., Yu, Z. and Zheng, H., 2015. A two-stage traveling-wave thermoacoustic electric generator with loudspeakers as alternators. *Applied Energy*, *137*, pp.9-17.

Kim, S., Choi, K., Lee, K. and Kim, K., 2016. Evaluation of automotive waste heat recovery for various driving modes. *Energy*, *106*, pp.579-589.

Kitadani, Y., Sakamoto, S.I., Sahashi, K. and Watanabe, Y., 2010. Basic study for practical use of thermoacoustic electric generation system.*system*, *1*, p.5.

Li, D., Wu, Z., Luo, E. and Zhang, L., 2014. Experimental Investigation on the Conversion between Heat and Power of the kW-class Thermoacoustic Engine. *Energy Procedia*, *61*, pp.1058-1062.

Orr, B., Akbarzadeh, A., Mochizuki, M. and Singh, R., 2015. A review of car waste heat recovery systems utilising thermoelectric generators and heat pipes. *Applied Thermal Engineering*, Volume 101, 25 May 2016, Pages 490–495.

Piccolo, A., 2017. Design issues and performance analysis of a two-stage standing wave thermoacoustic electricity generator. *Sustainable Energy Technologies and Assessments*, in press, https://doi.org/10.1016/j.seta.2016.10.011.

Swift, G.W., 2000, July. Streaming in thermoacoustic engines and refrigerators. In *NONLINEAR ACOUSTICS AT THE TURN OF THE MILLENNIUM: ISNA 15, 15th International Symposium* (Vol. 524, No. 1, pp. 105-114). AIP Publishing.

Swift, G.W., 2002. *Thermoacoustics*. Acoustical society of America.

Ward B, Clark J and Swift G., 2012. Design Environment for Low-amplitude Thermoacoustic Energy Conversion DeltaEC Version 6.3 b11 Users Guide. Los Alamos National Laboratory.

Wu, Z., Yu, G., Zhang, L., Dai, W. and Luo, E., 2014. Development of a 3kW double-acting thermoacoustic Stirling electric generator. *Applied Energy*, *136*, pp.866-872.

Yazaki, T., Iwata, A., Maekawa, T. and Tominaga, A., 1998. Traveling wave thermoacoustic engine in a looped tube. *Physical Review Letters*, *81*(15), p.3128.

Yang, Z., Zhuo, Y., Ercang, L. and Yuan, Z., 2014. Travelling-wave thermoacoustic high-temperature heat pump for industrial waste heat recovery. *Energy*, *77*, pp.397-402.

Yu, Z.B., Li, Q., Chen, X., Guo, F.Z. and Xie, X.J., 2005. Experimental investigation on a thermoacoustic engine having a looped tube and resonator. *Cryogenics*, *45*(8), pp.566-571.

Yu, Z., Backhaus, S. and Jaworski, A.J., 2009. Design and testing of a travelling-wave looped-tube engine for low-cost electricity generators in remote and rural areas. *American Institute of Aeronautics and Astronautics*.

Yu, Z., Jaworski, A.J. and Backhaus, S., 2010. A low-cost electricity generator for rural areas using a travelling-wave looped-tube thermoacoustic engine. *Proceedings of the Institution of Mechanical Engineers, Part A: Journal of Power and Energy*, *224*(6), pp.787-795.

Yu, Z., Jaworski, A.J. and Backhaus, S., 2012. Travelling-wave thermoacoustic electricity generator using an ultra-compliant alternator for utilization of low-grade thermal energy. *Applied Energy*, *99*, pp.135-145.

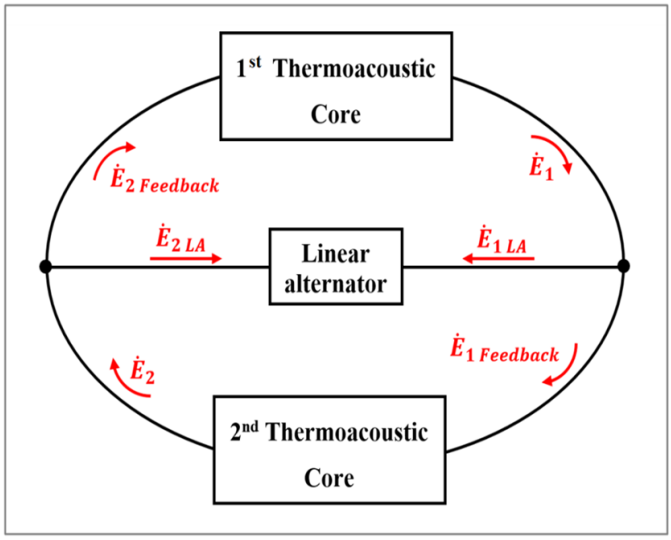

Figure 1: *Conceptual drawing of the proposed two-stage engine.*

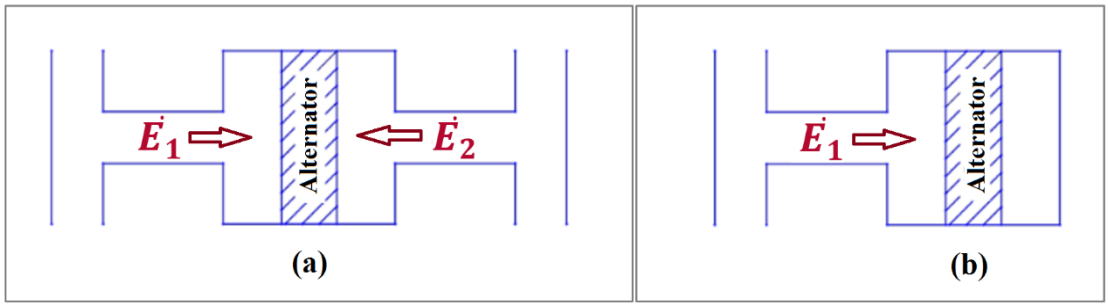

Figure 2: *Linear alternator coupling configurations (a) push-pull (b) compliance housing*

Table 1: *Linear alternator specifications (Q-Drive 1S132M)*

Parameter	**Value**
Stator resistance	2 ohm DC
Stator inductance	46 mH
Ratings	110 VAC rms @ 60 Hz/4.0 A rms
Stroke limit	14 mm
Nominal BL product	47 N/Ampere (approximate)
Intrinsic Stiffness	6 kN/m (approximate)
Damping, Rm	7.0 N-s/m (approximate)
Moving mass	0.721kg
Piston area	1385.4 mm^2

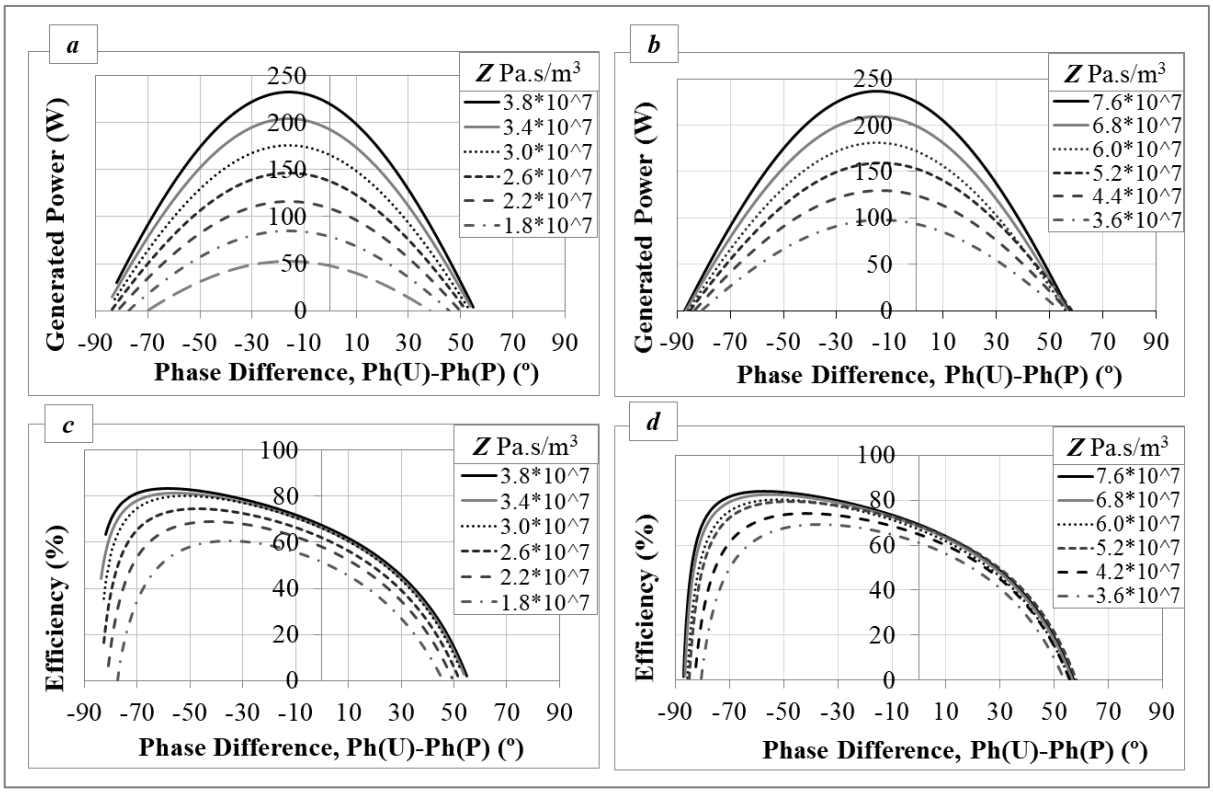

Figure 3: *(a) LA performance at push-pull coupling and (b) LA performance at compliance housing coupling (c) LA efficiency at push-pull coupling (d) LA efficiency at compliance housing.*

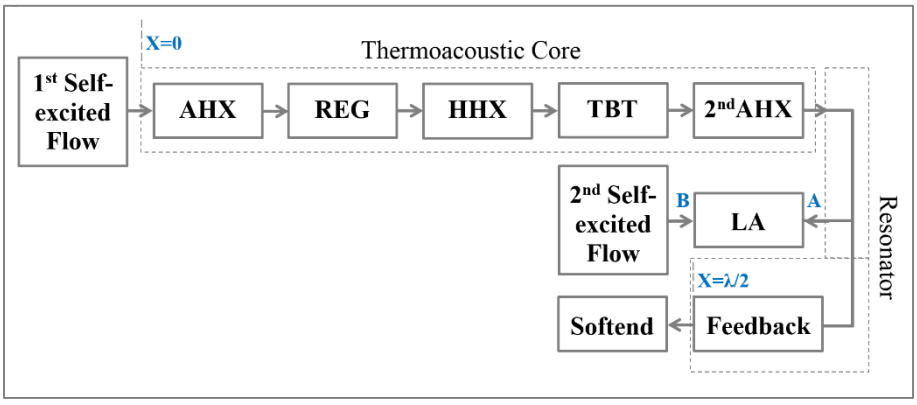

Figure 4: *Block diagram of the segments in the DeltaEC simulation: ambient heat exchanger (AHX), regenerator (REG), hot heat exchanger (HHX), thermal buffer tube (TBT), secondary cold heat exchanger (2ndAHX), feedback pipe (Feedback), linear alternator (LA).*

Table 2: *Some of the investigated parameters of thermoacoustic engine*

Component	**Parameter (unit)**	**Range**	**Optimized Value**
Core area / Feedback area	Ratio	3.5-7.5	6
Core	Diameter (mm)	75-125	102.2
AHX	Length (mm)	20-40	30
	Porosity (%)	20-40	29.2
	Plate Spacing (mm)	0.5-5	1
Regenerator	Length (mm)	50-90	73
	Porosity (%)	70-90	79.9
	δ_k/r_h	4-7	5.1
HHX	Length (mm)	20-60	40
	Porosity (%)	10-50	34.4
	Fin Spacing (mm)	0.5-2.5	1
TBT	Length (mm)	90-240	162
2^{nd}AHX	Length (mm)	10-30	20
	Porosity (%)	20-40	30.5
	Plate Spacing (mm)	0.5-5	1
Feedback loop	Diameter (mm)	38-43	40.8
	Length (mm)	6500-8500	7200

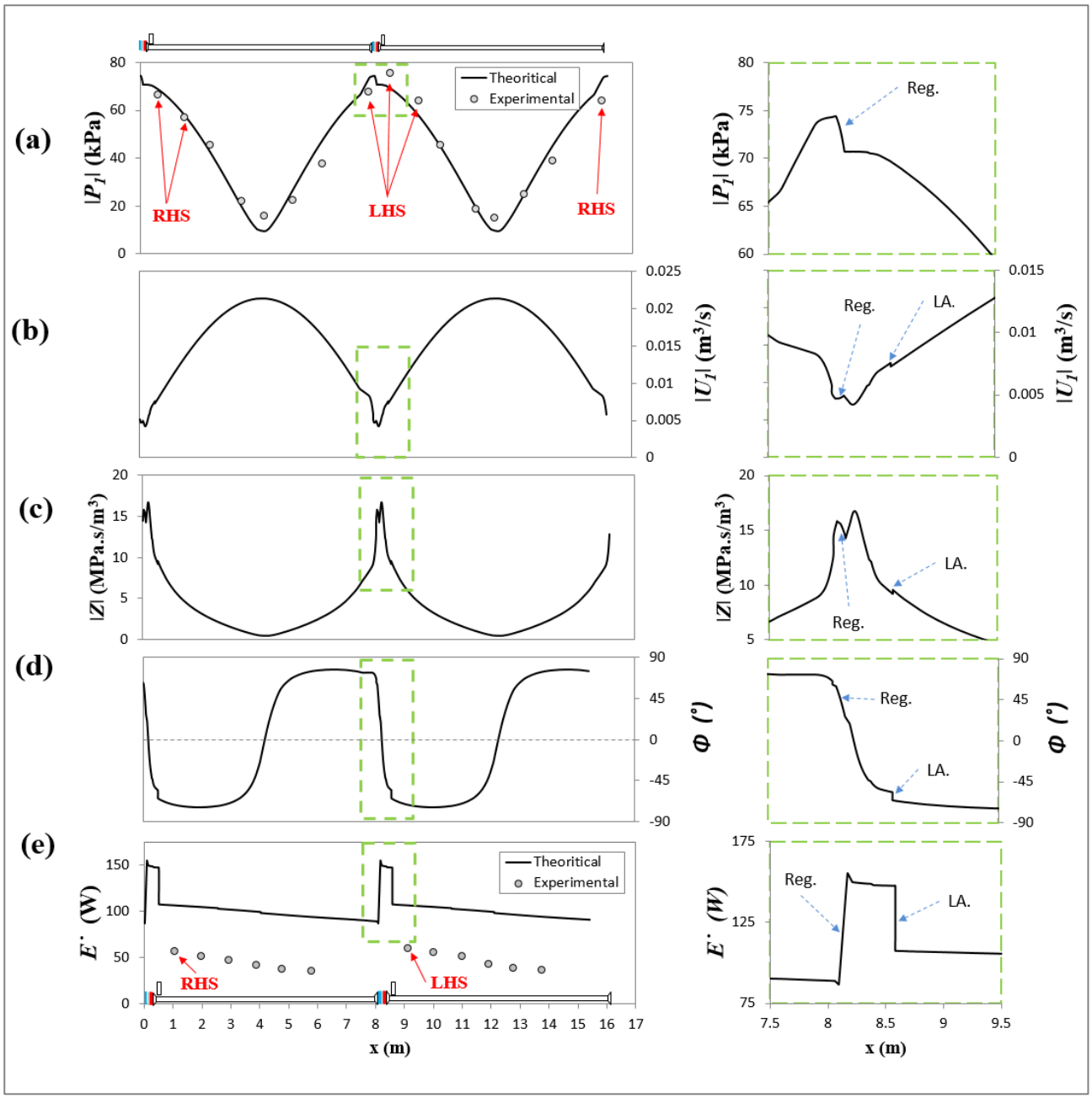

Figure 5: *Simulation results (a) pressure amplitude, (b) volumetric velocity, (c) acoustic impedance, (d) phase difference angle and (e) acoustic power flow along the engine.*

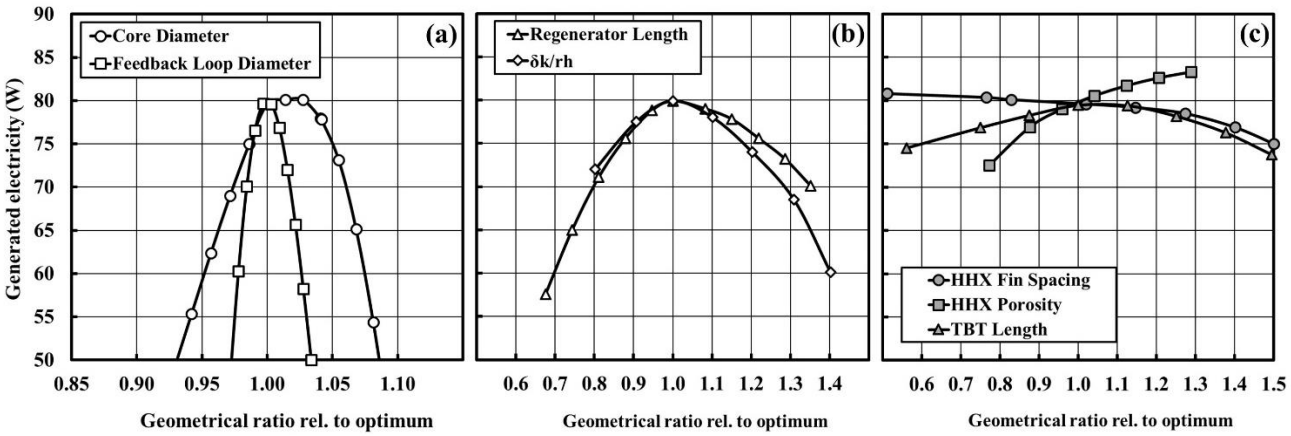

Figure 6: *Results of sensitivity analysis: (a) core and feedback loop diameters; (b) regenerator length and δ_k/r_h; (c) TBT length and HHX parameters*

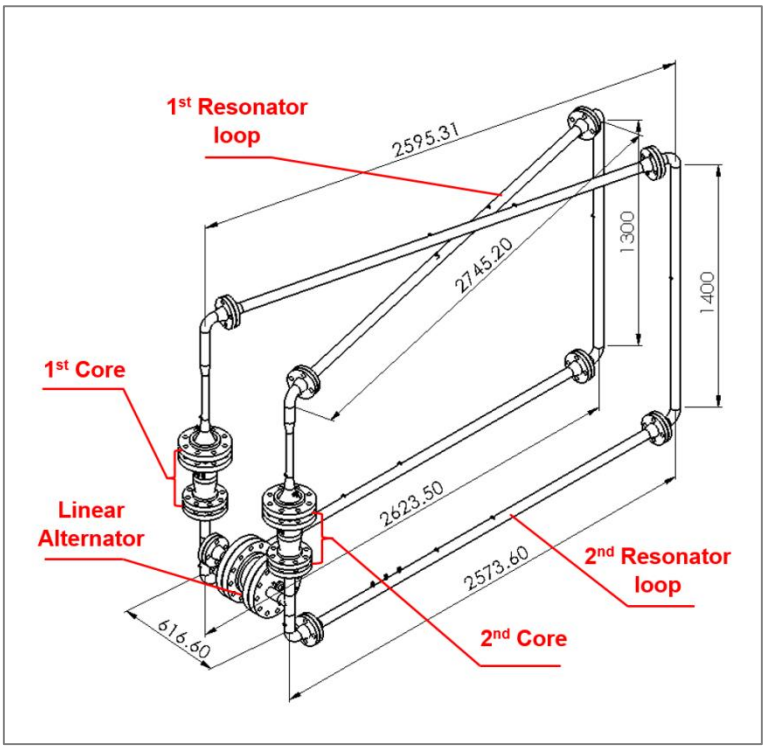

Figure 7: *Schematic layout of the experimental apparatus with basic dimensions.*

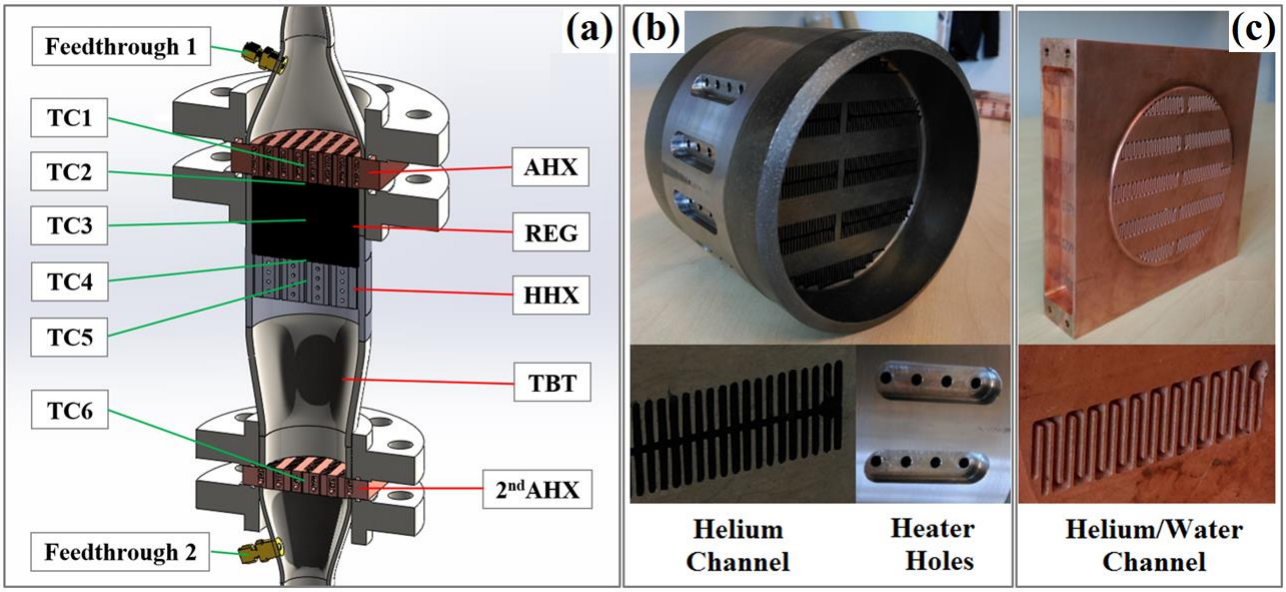

Figure 8: *Thermoacoustic core; (a) cross-section showing AHX, REG, HHX, TBT and 2ndAHX, (b) details of HHX, (c) details of AHXs.*

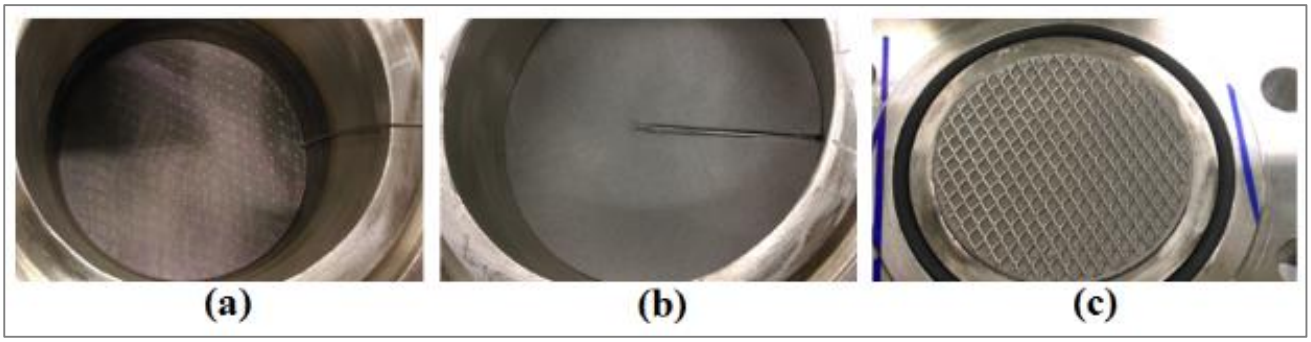

Figure 9: *Regenerator stacking stages (a) one screen; (b) half filled; (c) full regenerator. 1.3 mm thick coarse mesh layers on both sides act as spacers.*

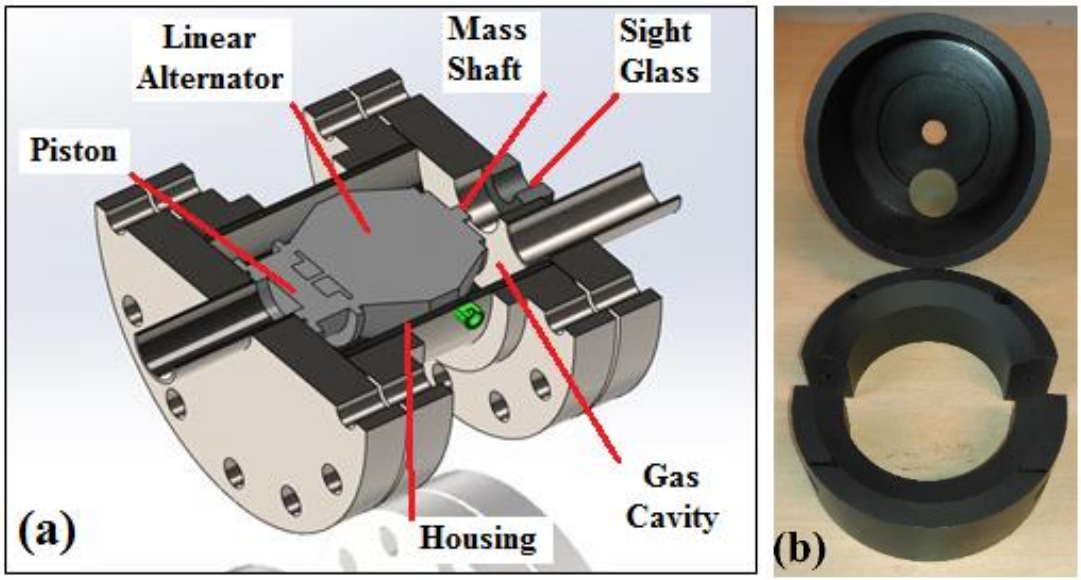

Figure 10: *(a) linear alternator housing; (b) plastic inserts to reduce dead volume.*

Table 3: *Dimensions and Materials Summary*

Part	Length (mm)	Inside Dia. (mm)	Material
AHX	30	102.2	Copper
Regenerator	73	102.0	Stainless Steel
HHX	40	102.2	Mild Steel
TBT-1st part	30	102.2	Stainless Steel
TBT-2nd part	102	102.2-77.9	Stainless Steel
TBT-3rd part	30	77.9	Stainless Steel
2ndAHX	20	77.4	Copper
Reducer	89	40.8	Stainless Steel
Tube	100	40.8	Stainless Steel
T-branch	114	40.8	Stainless Steel
Feedback-1st part	6880	40.8	Stainless Steel
Reducer	64	40.8-26.5	Stainless Steel
Feedback-2nd part	275	26.5	Stainless Steel
Enlargement	166	26.5-102.2	Stainless Steel
LA Branches	200,120	40.8	Stainless Steel
LA Housing	175	154.1	Stainless Steel

Figure 11: *The actual build of the demonstrator rig as set up in the laboratory.*

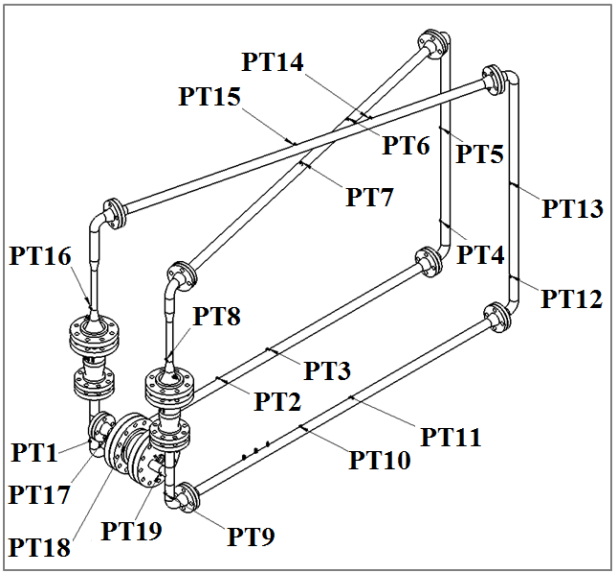

Figure 12: *Distribution of pressure transducer ports along the engine loop.*

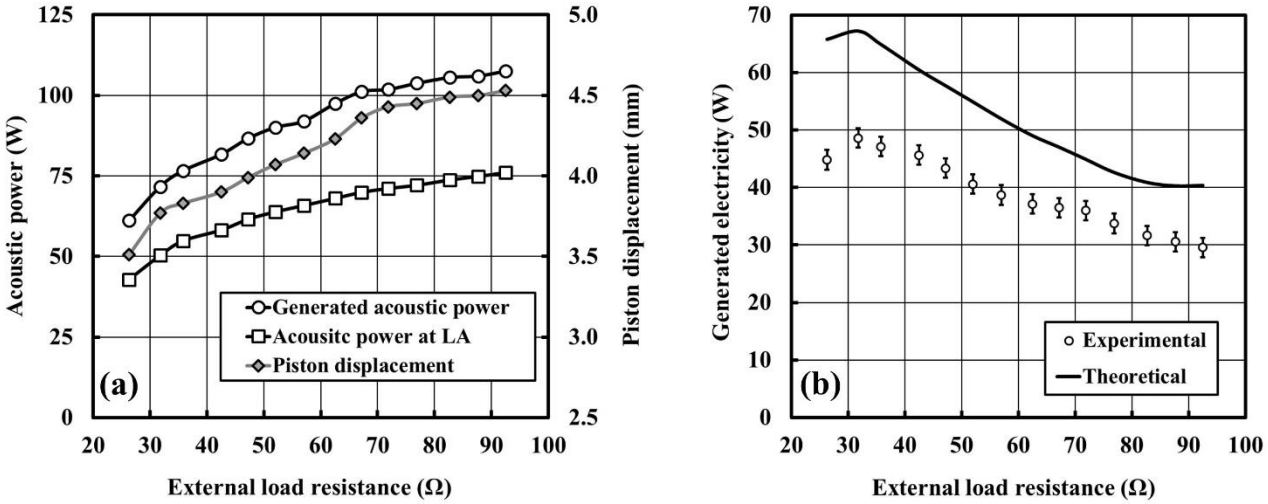

Figure 13: *(a) The generated acoustic power in one stage, the acoustic power on one side of the linear alternator and the piston displacement, (b) the electricity generated by the engine, when the load resistance on the linear alternator is varied*

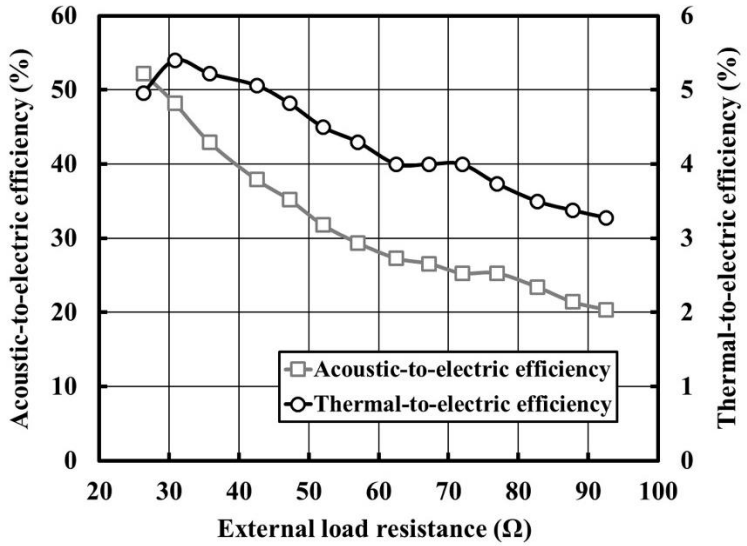

Figure 14: *Effect of load resistance on acoustic-to-electric and thermal-to-electric efficiencies.*

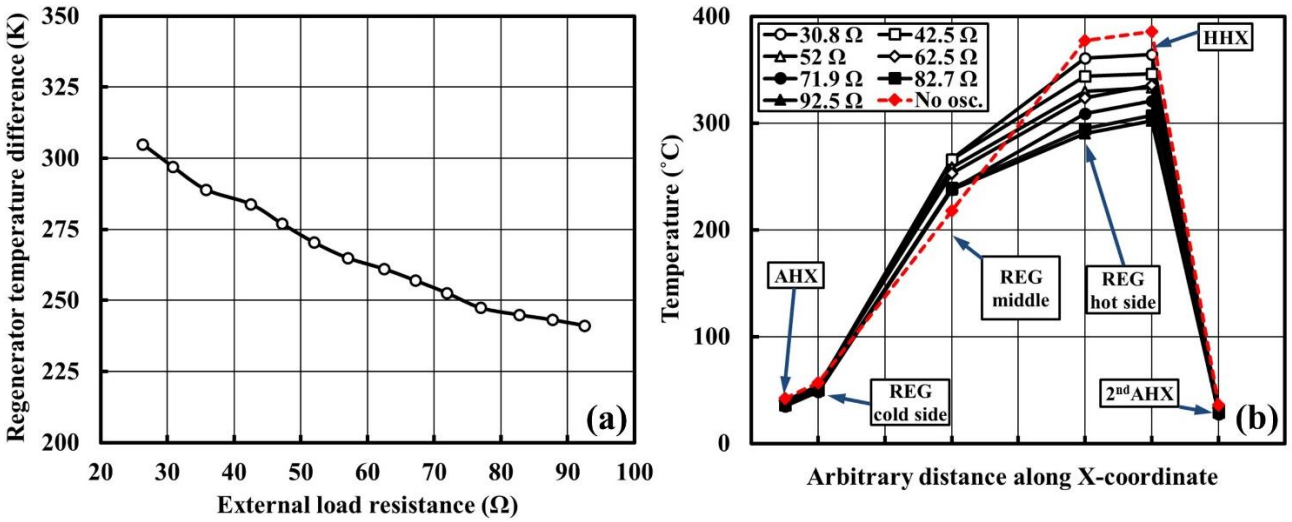

Figure 15: *(a) Effect of load resistance on temperature difference across the regenerator; (b) Temperature distribution along the thermoacoustic core at different load resistance values. Red line shows temperature distribution prior to onset of oscillations.*